



Diffusive dynamics during the high-to-low density transition in amorphous ice

Fivos Perakis^{a,b,1}, Katrin Amann-Winkel^{a,1}, Felix Lehmkuhler^{c,d}, Michael Sprung^c, Daniel Mariedahl^a, Jonas A. Sellberg^e, Harshad Pathak^a, Alexander Späh^a, Filippo Cavalca^{a,b}, Daniel Schlesinger^{a,2}, Alessandro Ricci^c, Avni Jain^c, Bernhard Massani^f, Flora Aubree^f, Chris J. Benmore^g, Thomas Loerting^f, Gerhard Grübel^{c,d}, Lars G. M. Pettersson^a, and Anders Nilsson^{a,3}

^aDepartment of Physics, AlbaNova University Center, Stockholm University, S-10691 Stockholm, Sweden; ^bSLAC National Accelerator Laboratory, Menlo Park, CA 94025; ^cDeutsches Elektronen-Synchrotron (DESY), 22607 Hamburg, Germany; ^dHamburg Centre for Ultrafast Imaging, 22761 Hamburg, Germany; ^eBiomedical and X-ray Physics, Department of Applied Physics, AlbaNova University Center, KTH Royal Institute of Technology, S-10691 Stockholm, Sweden; ^fInstitute of Physical Chemistry, University of Innsbruck, A-6020 Innsbruck, Austria; and ^gX-ray Science Division, Advanced Photon Source, Argonne National Laboratory, Argonne, IL 60439

Edited by Pablo G. Debenedetti, Princeton University, Princeton, NJ, and approved May 31, 2017 (received for review March 31, 2017)

Water exists in high- and low-density amorphous ice forms (HDA and LDA), which could correspond to the glassy states of high- (HDL) and low-density liquid (LDL) in the metastable part of the phase diagram. However, the nature of both the glass transition and the high-to-low-density transition are debated and new experimental evidence is needed. Here we combine wide-angle X-ray scattering (WAXS) with X-ray photon-correlation spectroscopy (XPCS) in the small-angle X-ray scattering (SAXS) geometry to probe both the structural and dynamical properties during the high-to-low-density transition in amorphous ice at 1 bar. By analyzing the structure factor and the radial distribution function, the coexistence of two structurally distinct domains is observed at $T = 125$ K. XPCS probes the dynamics in momentum space, which in the SAXS geometry reflects structural relaxation on the nanometer length scale. The dynamics of HDA are characterized by a slow component with a large time constant, arising from viscoelastic relaxation and stress release from nanometer-sized heterogeneities. Above 110 K a faster, strongly temperature-dependent component appears, with momentum transfer dependence pointing toward nanoscale diffusion. This dynamical component slows down after transition into the low-density form at 130 K, but remains diffusive. The diffusive character of both the high- and low-density forms is discussed among different interpretations and the results are most consistent with the hypothesis of a liquid–liquid transition in the ultraviscous regime.

liquid–liquid transition | glass transition | amorphous ice | X-ray photon-correlation spectroscopy | supercooled water

It has been postulated that water's hydrogen-bonding network can exist in two liquid forms of different density, namely high- and low-density liquid water (HDL and LDL, respectively) (1). These forms were recently simulated as metastable free-energy basins and a liquid–liquid transition was observed in the ST2 molecular model of water (2), but direct experimental evidence is still missing. Furthermore, it is hypothesized that the observed high- and low-density amorphous ice forms (HDA and LDA, respectively) are the glassy counterparts of the two liquid forms found deeply in the metastable supercooled regime (3). The HDA-to-LDA transition has been proposed to be a first-order phase transition (4–8) and could occur in the ultraviscous liquid state at temperatures above the glass transition (9). Similar observations have been reported by studying water confined in protein crystals and aqueous solutions (10, 11), which indicate the occurrence of the transition between two viscous liquid states of water. However, there is contradicting evidence that the transition from HDA to LDA involves several intermediate forms (12, 13) and it is questioned whether the amorphous ices are thermodynamically linked with supercooled water (14, 15). Based on experimental studies using calorimetry (9, 16–18), dielectric spectroscopy (9, 19), isotope

exchange (20), and diffusion in amorphous solid water (ASW) (21, 22), it was suggested that there is a glass–liquid transition in LDA around $T_{g\text{ LDA}} \sim 136$ K (heating rate 30 K/min) (16). In addition, there have been indications of a glass–liquid transition in HDA at elevated pressures (23, 24), as well as at ambient pressure at $T_{g\text{ HDA}} \sim 116$ K (heating rate 10 K/min) (9). Several alternative interpretations have been proposed involving an orientational glass transition (25) or crystal-like behavior (14, 26, 27), which would rule out the appearance of translational diffusion at the previously proposed glass transition.

To address the open questions concerning the nature of the glass transition and hypothesized polymorphism of water, we use experimental X-ray techniques that probe the structure and dynamics of amorphous ice, as HDA transitions to the low-density form at ambient pressure. The experimental setup is shown in Fig. 1*A*, where the diffraction pattern was recorded both in wide- and small-angle X-ray scattering (WAXS and SAXS, respectively) geometry. Using X-ray diffraction at WAXS geometry, one can distinguish between the high- and low-density forms (Fig. 1*B*) due to changes in the static structure factor $S(Q)$, with

Significance

The importance of a molecular-level understanding of the properties, structure, and dynamics of liquid water is recognized in many scientific fields. It has been debated whether the observed high- and low-density amorphous ice forms are related to two distinct liquid forms. Here, we study experimentally the structure and dynamics of high-density amorphous ice as it relaxes into the low-density form. The unique aspect of this work is the combination of two X-ray methods, where wide-angle X-ray scattering provides the evidence for the structure at the atomic level and X-ray photon-correlation spectroscopy provides insight about the motion at the nanoscale, respectively. The observed motion appears diffusive, indicating liquid-like dynamics during the relaxation from the high- to low-density form.

Author contributions: F.P., K.A.-W., F.L., M.S., A.R., T.L., G.G., and A.N. designed research; F.P., K.A.-W., F.L., M.S., D.M., J.A.S., H.P., A.S., F.C., A.R., A.J., B.M., F.A., C.J.B., T.L., and A.N. performed research; F.P., K.A.-W., D.M., and D.S. analyzed data; and F.P., K.A.-W., L.G.M.P., and A.N. wrote the paper.

The authors declare no conflict of interest.

This article is a PNAS Direct Submission.

Freely available online through the PNAS open access option.

See Commentary on page 8141.

¹F.P. and K.A.-W. contributed equally to this work.

²Present address: Department of Environmental Science and Analytical Chemistry & Bolin Centre for Climate Research, Stockholm University, 114 18 Stockholm, Sweden.

³To whom correspondence should be addressed. Email: andersn@fysik.su.se.

This article contains supporting information online at www.pnas.org/lookup/suppl/doi:10.1073/pnas.1705303114/-DCSupplemental.

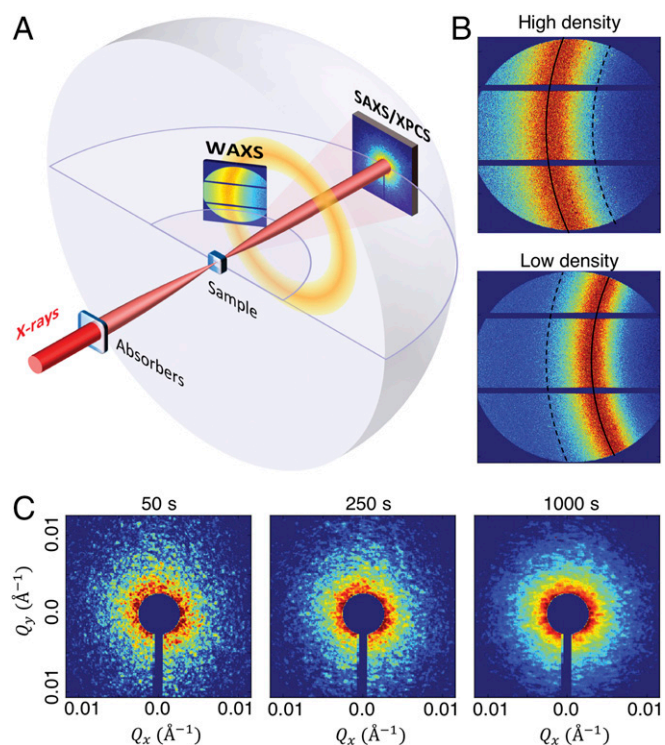


Fig. 1. Coherent X-ray diffraction setup combining WAXS with XPCS in SAXS. (A) The experimental scattering geometry that was used employs two detectors for WAXS and SAXS, respectively. (B) The WAXS scattering pattern allows distinguishing high- and low-density forms; the lines indicate the position of the maxima at momentum transfer $Q = 1.7 \text{ \AA}^{-1}$ and 2.1 \AA^{-1} . (C) The scattering pattern recorded in SAXS geometry is used to extract the dynamics with XPCS. Here the speckle patterns for different exposure times at temperature $T = 89 \text{ K}$ are shown.

Q being the momentum transfer. In the SAXS geometry, we use X-ray photon-correlation spectroscopy (XPCS) (28–30), which is based on the observation of X-ray speckle patterns that arise due to the interference of X-rays scattered off density heterogeneities within the illuminated volume (31) (Fig. 1C). In the low- Q range, changes in the speckle pattern reflect the dynamics at the nanometer length scale. For longer exposure time the speckle contrast is gradually lost due to dynamics in the sample, giving rise to a more uniform scattering pattern (Fig. 1C). The corresponding diffusion constants can be evaluated on the nanoscale through the Q dependence of the characteristic time constant (29).

Structural Information from WAXS

The WAXS data were recorded using high-photon energies of 100 keV (*Materials and Methods*). The first $S(Q)$ diffraction peak of HDA is observed at $Q = 2.1 \text{ \AA}^{-1}$ (Fig. 2A) and with increasing temperature, a second peak appears at $Q = 1.7 \text{ \AA}^{-1}$. Using unannealed HDA (6) (uHDA) the first diffraction peak shifts toward the LDA position upon warming, involving several intermediate states (Fig. 2A and *SI Appendix*). This is consistent with previous X-ray scattering studies where no isosbestic point was observed (12, 13, 32), referring to points where $S(Q)$ is constant with temperature. Instead, using an annealed form of HDA (6, 7) (equilibrated HDA, eHDA) we observe two distinct peaks, without any intermediate peak positions (see also *SI Appendix*), which exhibit an isosbestic point at $Q = 1.9 \text{ \AA}^{-1}$ followed by several crossings at higher Q s (Fig. 2B). The total X-ray scattering radial distribution function $g(r)$, obtained by Fourier-transforming $S(Q)$ (*Materials and Methods*), is shown in Fig. 2C, with r being the interatomic distance. Upon heating, $g(r)$ decreases between the first

and second coordination shell ($r \approx 3.5 \text{ \AA}$), indicating loss of interstitial molecules and increased tetrahedral contribution in the low-density form (33) with an isosbestic point at 4.15 \AA .

The complex shift observed in uHDA is attributed to strain release and large interface scattering of interpenetrating structures, and the transition to the low-density form involves several intermediate states (32). In eHDA the observed double peak in $S(Q)$ indicates coexistence of high- and low-density domains, as suggested by earlier experimental (5, 7) and theoretical investigations (15). In this case, the decomposition of both the static structure factor and the radial distribution function into the sum of two components can be justified by assuming that the contribution of interfaces to the scattering is negligible due to the large domain sizes. The temperature dependence of $S(Q)$ (Fig. 2) signifies the transition of HDA to a low-density form. The question is whether this transition occurs between amorphous ice forms, i.e., an HDA-to-LDA transition, or whether the transition occurs between two liquid states, inferring instead an HDL-to-LDL transition in the ultraviscous regime. Another possibility would be that the transition involves both the liquid and glassy forms (such as HDL→LDL→LDA or HDL→LDA→LDL). Such cases cannot be distinguished purely from the static structure factor and therefore dynamical information like the intermediate scattering function accessible by XPCS is needed.

Dynamical Information from XPCS

The XPCS data at SAXS geometry were measured at a photon energy of 8.4 keV (*Materials and Methods*). The pronounced signal at small scattering angles of $Q \sim 0.01 \text{ \AA}^{-1}$ reflects nanometer length-scale heterogeneities presumably due to the grainy nanostructure of the sample. Previous neutron-scattering studies discuss structural heterogeneities as a result of scattering in the Porod-limit region (13) ($Q \sim 0.1 \text{ \AA}^{-1}$), which is beyond the scope

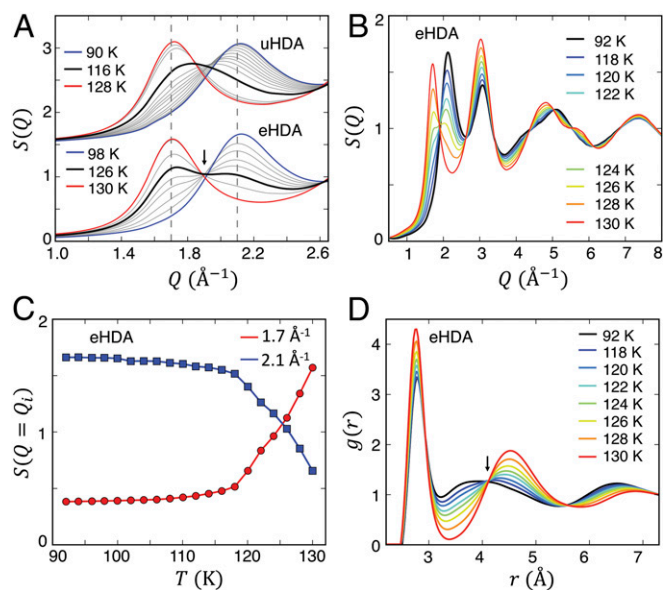


Fig. 2. Structural information obtained by the static structure factor $S(Q)$ and radial distribution function $g(r)$. (A) Comparison of the structure factor of the uHDA and annealed eHDA forms. The black solid line highlights the difference in behavior between eHDA with an isosbestic point and uHDA with a continuously shifting peak. (B) The extended static structure factor $S(Q)$ at different temperatures, during the transition from the high- to low-density form. (C) The amplitude of $S(Q)$ at $Q = 1.7 \text{ \AA}^{-1}$ (red circles) and $Q = 2.1 \text{ \AA}^{-1}$ (blue squares) as a function of temperature. (D) The radial distribution functions $g(r)$ for different temperatures, where the isosbestic point at $r = 4.15 \text{ \AA}$ is indicated by the arrow.

of the present study. The present XPCS measurement is performed in the Q range of $0.003\text{--}0.01\text{ \AA}^{-1}$, a wave-vector range inaccessible to visible light (34), which is connected to structural rearrangements on the $\sim 100\text{-nm}$ length scale (35, 36). The dynamics are recorded by measuring the temporal autocorrelation function $g_2(Q, \delta t)$ where δt is the correlation time, which can be related to the intermediate scattering function $F(Q, \delta t)$ through

$$g_2(Q, \delta t) = \beta |F(Q, \delta t)|^2 + 1,$$

where β is the speckle contrast that depends on the experimental parameters.

Fig. 3 *A* and *B* shows the WAXS scattering patterns that were recorded giving the static structural information and the $|F(Q, \delta t)|^2$ dynamics measured in SAXS geometry. Here, the displayed $I(Q)$ and $|F(Q, \delta t)|^2$ shown were recorded at the same sample position, using two detectors at different scattering angles. The $|F(Q, \delta t)|^2$ data are fitted with a double-exponential function (*Materials and Methods*), which at $T = 89\text{ K}$ yields a single time constant, whereas at temperatures $T > 110\text{ K}$ it captures an additional faster component. The WAXS scattering pattern at 130 K changed during the XPCS measurement (Fig. 3*A*), as indicated by the pattern recorded before (solid line) and after (dashed line) the XPCS measurement. In Fig. 3*B*, at 130 K the solid and dashed lines depict the fits at early and late times, respectively, during the high-to low-density transition (the first $0\text{--}400\text{ s}$ and last $700\text{--}1,000\text{ s}$ of the total $1,000\text{ s}$ recorded), which is accompanied by a heat release during the transformation (*SI Appendix*).

Two-time temporal correlation maps $C(Q, \delta t, t)$ (28, 37–40) (Fig. 3*C*; *Materials and Methods*) provide a very sensitive measure of the underlying dynamics and allow resolving whether the system

exhibits dynamical heterogeneities, or if the recorded dynamics are homogeneous. In the former case the linewidth of $C(Q, \delta t, t)$ would fluctuate during the measurement time t ; in the latter, the width would remain constant. For $T = 89\text{ K}$ the $C(Q, \delta t, t)$ exhibits fluctuations with a multitude of relaxation times, whereas at $T = 125\text{ K}$, the dynamics speed up during the measurement. At 130 K dynamics are initially fast and more homogeneous (region 1) but after $\sim 400\text{ s}$ a transition to slower and more heterogeneous dynamics is observed (regions 2 and 3).

The time constants τ obtained by the double-exponential fit are shown in Fig. 4*A*. The slower component appears nearly temperature-independent, whereas the faster component manifested at $T = 115\text{ K}$ accelerates $\sim 100\text{-fold}$ upon heating to $T = 130\text{ K}$. The relative amplitudes of the two components change with increasing temperature $T > 110\text{ K}$, with the slow component gradually decaying and the fast component gaining in amplitude, shown in *SI Appendix*, Fig. S7. At $T = 130\text{ K}$ the time constants obtained for the initial $0\text{--}400\text{ s}$ (1) and the final $700\text{--}1,000\text{ s}$ (3) are shown, connected by arrows to indicate the time ordering.

The solid and dashed lines in Fig. 4*A* are obtained from Arrhenius fits (*Materials and Methods*). A similar trend is seen by the normalized variance χ_T extracted from the $C(Q, \delta t, t)$ (38), which is an experimental estimator of the four-point dynamical susceptibility (41). The amplitude of χ_T of $C(Q, \delta t, t)$ (Fig. 4*B*) is proportional to the relative width $\Delta\tau/\tau$ of the characteristic relaxation time; the maximum peak value χ_0 is thus a measure of the dynamical heterogeneities in the system. Fig. 4*B* (*Inset*) shows an abrupt decay in χ_0 for $T > 115\text{ K}$, indicating a transition to a more dynamically homogeneous regime.

With XPCS in the low- Q regime one can derive the diffusion constant on nanometer length scales by the Q dependence of the characteristic time constant (29). For hyperdiffusion or ballistic

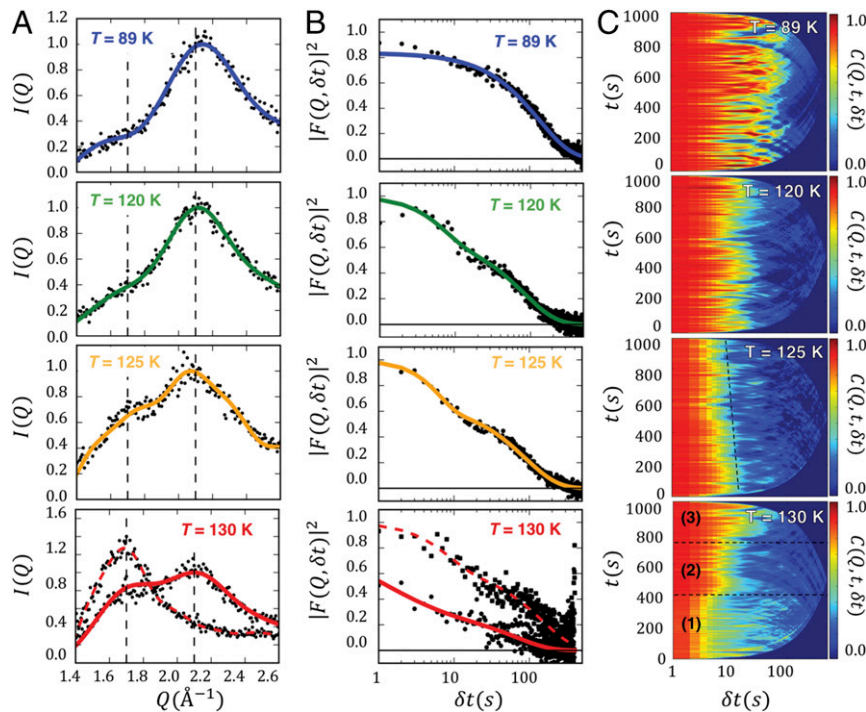


Fig. 3. Dynamical information obtained through the intermediate scattering function $F(Q, \delta t)$. (A) The angularly integrated intensity in WAXS geometry at different temperatures. The solid and dashed lines at $T = 130\text{ K}$ indicate the scattering intensity recorded in the beginning and at the end of the measured dynamics, respectively. (B) The intermediate scattering function $|F(Q, \delta t)|^2$ at different temperatures recorded in SAXS geometry at $Q = 0.01\text{ \AA}^{-1}$. The solid and dashed lines at $T = 130\text{ K}$ indicate double-exponential fits recorded during the initial 400 s (solid line) and final 300 s (dashed line) of the total $1,000\text{-s}$ trace. (C) The two-time temporal autocorrelation $C(Q, \delta t, t)$ for different temperatures at $Q = 0.01\text{ \AA}^{-1}$. At lower temperatures, a large variation of timescales is observed along δt . At $T = 125\text{ K}$ one can see a gradual acceleration indicated by the dashed line. At $T = 130\text{ K}$ the dynamics change during the measurement and the dashed lines indicate regions (1), (2), and (3), which are analyzed separately.

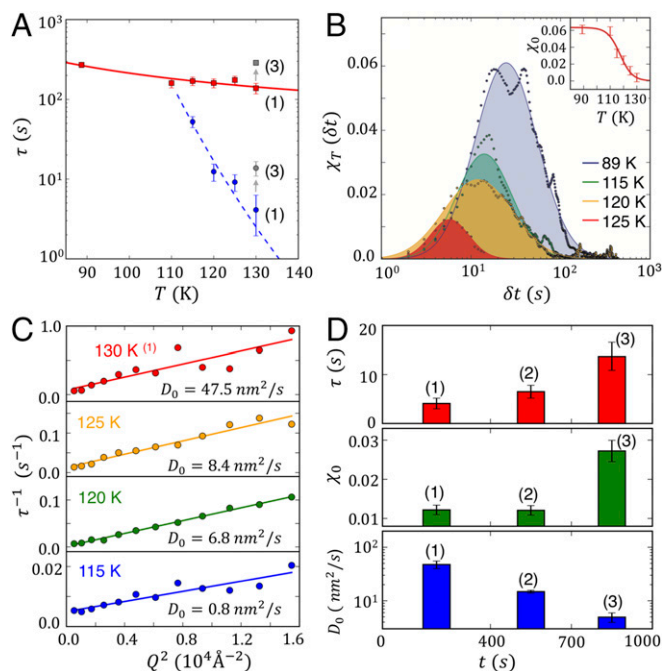


Fig. 4. Evidence for diffusive dynamics in the ultraviscous regime. (A) The time constants obtained from the double-exponential fit of $|F(Q, \delta t)|^2$ at different temperatures at $Q = 0.01 \text{ \AA}^{-1}$. For the lower temperatures ($T = 89$ and 110 K) only a single, slow component is obtained (red squares), whereas at higher temperatures a second, faster component appears (blue circles). The solid and dashed lines depict the results of two Arrhenius fits and the error bars are the SE. (B) The normalized variance χ_T obtained from $C(Q, \delta t, t)$ at different temperatures, where the solid lines are Gaussian fits (with logarithmic x axis) used to quantify the maximum peak amplitude χ_0 . (Inset) The χ_0 for all temperatures. (C) The fast time constant obtained from the double exponential fit plotted as $1/\tau$ over Q^2 . The solid lines depict the result of a fit $1/\tau \sim D_0 Q^2$, where D_0 is the diffusion constant at different temperatures. At 130 K the data shown are for the shorter interval $0\text{--}400 \text{ s}$, thus the resulting increase in noise. (D) At 130 K , the obtained time constant of the faster component τ increases as a function of measurement time t , and so does the χ_0 , whereas the diffusion constant decreases with t .

motion τ exhibits $1/\tau \sim Q$ dependence, whereas $1/\tau \sim Q^2$ dependence is typical for diffusion, with the diffusion constant D_0 as the proportionality constant. Fig. 4C shows the $1/\tau$ versus Q^2 for temperatures of 115 K and above. At temperatures below 115 K and for the slow component no Q^2 dependence is observed. This observation indicates that the slow component is not diffusive and can be associated with viscoelastic relaxation due to release of inner stresses and convective flow (29, 42). From the fits in Fig. 4C D_0 is determined for the fast component to vary from 0.8 to $47.5 \text{ nm}^2/\text{s}$ at $115\text{--}130 \text{ K}$. No corresponding faster fluctuation or diffusive dynamics are observed in crystalline ice as discussed in *SI Appendix, Fig. S8*.

Discussion

It is essential to discuss whether the experimental evidence provides further insight about the glass transition and whether the observed high-to-low-density transition occurs between amorphous or liquid states. The glass-transition temperature T_g depends on the heating rate (*SI Appendix*). Previous investigations using calorimetry proposed $T_{g \text{ HDA}} \sim 116 \text{ K}$ (9) using a heating rate of 10 K/min . In dielectric spectroscopy measurements, where a much slower heating rate was used, the glass-transition temperature for HDA was determined at $T_{g \text{ HDA}} = 110 \text{ K}$; the present heating rate is comparable to that used for the dielectric spectroscopy measurements. Therefore, we propose that the observed faster component at temperatures above 110 K (Fig.

4A), accompanied by the decrease of χ_0 , indicate a glass-to-liquid transition from HDA to HDL. Because the observed glass transition is kinetic in nature, the diffusivity exhibits continuous behavior during the transition. Therefore, we conclude that the reason for not observing the diffusive component below 110 K is that it occurs on a timescale longer than the experimental observation time, where the dynamics are dominated by the viscoelastic component. The acceleration of the dynamics at 125 K (Fig. 3C) is due to the ongoing HDA–HDL transition within the $1,000\text{-s}$ duration of the XPCS measurement. Because XPCS is measured in the SAXS geometry, it is sensitive to diffusion occurring due to structural rearrangements of the nanoscale heterogeneities. The diffusion involves translational motion at the nanometer length scale and therefore we can determine that the fast component does not reflect purely molecular reorientation, responsible for an orientational glass transition (25). However, there can be reorientation occurring, coupled to translational motion (43). We also conclude that the observed diffusive behavior near the glass transition would not manifest itself in a crystal-like amorphous ice (14, 26), but instead indicates that the amorphous matrix exhibits HDL-like dynamics.

In Fig. 4D, the dynamical properties are analyzed in three different time domains during the high-to-low-density transition. This transition is kinetically driven and accelerated due to the heat release, which is associated with a temperature rise on the order of 10 K (*SI Appendix*) and will therefore lead to a step-like change between regions 1 and 2. Directly after the jump between regions 1 and 2 (Fig. 4D), both τ and χ_0 increase and D_0 decreases, followed by a more significant change in region 3, whereas a similar behavior is seen from the angularly integrated SAXS signal (*SI Appendix, Fig. S6*). The data indicate that the transformation to the low-density form is completed upon entering region 2. The corresponding dynamics in region 2 still show diffusive characteristics and we therefore conclude that HDL transforms into LDL rather than LDA. The slowing down in region 3 can be explained by cooling after the heat release in combination with the difference in T_g between the high- and low-density forms, respectively, 110 and 126 K . This observation is consistent with the dielectric relaxation measurements, where a deceleration by a factor of ~ 100 was observed upon transforming HDA to the low-density state (9). However, it cannot be excluded that the observed deceleration is also due to the formation of small cubic ice nuclei with a size much below 10 nm , thus preventing detection in WAXS (44). The alternative of reversion into LDA form is not consistent with the observed diffusive dynamics (Fig. 4C) at the low-density form and therefore we derive that the final stage corresponds to the LDL state. The diffusivity obtained here is the strongest indication of liquid-like motion between 115 and 130 K and evidence for HDL and LDL. During the HDL-to-LDL transition at 130 K , the diffusion coefficients slow down by nearly an order of magnitude, from $48 \text{ nm}^2/\text{s}$ ($\sim 5 \times 10^{-17} \text{ m}^2/\text{s}$) for HDL to $5 \text{ nm}^2/\text{s}$ for LDL ($\sim 5 \times 10^{-18} \text{ m}^2/\text{s}$). The latter is in fair agreement with previous experiments on ASW using CO_2 ($\sim 8 \times 10^{-17} \text{ m}^2/\text{s}$ at 130 K) and molecular dynamics simulations ($\sim 1.5 \times 10^{-16} \text{ m}^2/\text{s}$ at 135 K) (45). The diffusion of ASW at the liquid/ice interface was measured using nanoscale films ($\sim 10^{-20} \text{ m}^2/\text{s}$ at 135 K) (21), which is considerably slower as the diffusivity in this case is presumably related to the mobility of molecules at the liquid/solid interface. Despite the difference in magnitude, the observed diffusivities exhibit a similar continuous trend across the ASW glass transition (21, 22). This interpretation was validated by measuring the LDA-to-LDL transition, where a diffusive component was observed at $T = 130 \text{ K}$ with nearly identical diffusion constants as those obtained in region 3 for LDL (*SI Appendix, Fig. S9*).

Summarizing our observations: (i) At temperatures $T < 110 \text{ K}$ a slow dynamical component is observed due to viscoelastic relaxation of HDA. (ii) Above 110 K a fast component appears exhibiting

diffusive character, which is attributed to the HDL. (iii) With increasing temperature HDA domains transform to HDL that further transform to the low-density form. (iv) During the high-to-low-density transition the dynamics slow down but remain diffusive, suggesting that the HDL is converting to LDL at 130 K. The question remains whether there exists also a stringent first-order phase transition at constant Gibbs free energy (8). Previous studies, varying pressure at temperatures above the glass transition, showed the presence of sharp boundaries between regions of HDA and LDA character (7, 46, 47). In accordance with these observations, our results point to the existence of a first-order phase transition between HDL and LDL, which can exist at higher temperature and under pressure (2). At ambient pressure, water's structure varies continuously upon cooling (44), but if there is an HDL-LDL phase transition at higher pressure, then the structural evolution will be discontinuous when crossing the transition. This would indicate the existence of a thermodynamic point at elevated pressures where the two forms can no longer be distinguished (1).

Materials and Methods

Sample Environment and Preparation. HDA ice can be prepared through different routes within the metastable phase diagram, and several substates that can be derived after annealing, heating, compression, and/or decompression at different temperatures have been named differently in the literature. We discriminate the preparation route of two most extreme cases, namely uHDA and eHDA ice. uHDA ice is prepared by direct pressure-induced amorphization of crystalline ice Ih at 77 K, i.e., without exceeding liquid nitrogen temperature (4, 6). The eHDA ice (7) is prepared by annealing uHDA at high pressure (1,100 MPa) with subsequent decompression to 70 MPa at 140 K, i.e., a region slightly above its glass-transition temperature T_g (9). This eHDA can be quench-recovered to ambient pressure and therefore studied as a metastable state within the stability region of LDA. With this experimental approach, we can probe the high-to-low-density transition by simply increasing the temperature at ambient pressure. The samples have been prepared by using a piston cylinder setup and a mechanical press (Zwick, Z100 TN).

For all measurements, a liquid N_2 -flow cryostat from JANIS was used. The amorphous ice samples were prepared and cold-loaded at liquid nitrogen temperature into the sample holder. A powdered sample was squeezed between two 50- μm -thick Kapton windows [WAXS at Advanced Photon Source (APS)] and 50- μm -thick diamond windows [XPCS at Deutsches Elektronen-Synchrotron (DESY)], respectively, resulting in a sample thickness of 2 mm (APS) or 1 mm (XPCS). The windows were held in place by a copper sample holder connected to the cold finger of the cryostat. The samples were measured in vacuum, i.e., without He-exchange gas. For the diffraction measurements at APS the cryostat was equipped with two Kapton windows and the pressure was $P < 1 \times 10^{-2}$ mbar. For the XPCS measurements the cryostat was connected directly to the beamline under vacuum without using additional windows.

WAXS Measurements and Data Analysis. X-ray diffraction measurements were performed at APS at beamline 6-ID-D using a 2D amorphous silicon area detector (Perkin-Elmer XRD1621) at $E = 100$ keV photon energy. CeO_2 powder was used for sample-detector distance calibration ($L = 348$ mm) and Q calibration. The 2D diffraction image, showing the typical water ring, was angularly integrated by using the software Fit2D (V.17.006) after applying polarization and geometrical corrections. The scattering intensity $I(Q)$ was corrected for background signal mainly from the Kapton windows and air measuring an empty sample holder and applied corrections for multiple scattering, detector efficiency, oblique incidence, and self-absorption (48). The static structure factor and the radial distribution function were calculated as described elsewhere (49). The $I(Q)$ data were normalized to the molecular form factor and the Compton scattering was subtracted. The total structure factor $S(Q)$ is given by

$$S(Q) - 1 = \frac{I(Q) - FF(Q)}{WF(Q)},$$

where $FF(Q)$ corresponds to the molecular form factor and $WF(Q)$ to the weighting factor. The radial distribution function $g(r)$ is calculated by a Fourier transformation of the static structure factor $S(Q)$:

$$g(r) = 1 + \frac{1}{2\pi^2 \rho r} \int_0^{Q_{\max}} M(Q, \Delta(r)) Q [S(Q) - 1] \sin(Qr) dQ,$$

where ρ is the number density per \AA^3 and $M(Q, \Delta(r))$ is a Lorch-like function

$$M(Q, \Delta(r)) = \frac{\sin(Q\Delta(r))}{Q\Delta(r)},$$

where $\Delta(r)$ is in the form

$$\Delta(r) = a \left[1 - \exp\left(-2.77 \left(\frac{r-r_1}{\omega_1}\right)^2\right) \right] + a \left[\frac{1}{2} + \frac{1}{\pi} \arctan\left(\frac{r-\omega_2}{\omega_2/2\pi}\right) \right] r^{0.5},$$

with parameters $a = \pi/Q_{\max}$, $r_1 = 2.8 \text{ \AA}$, $\omega_1 = 0.5 \text{ \AA}$, $\omega_2 = 12.0 \text{ \AA}$, and $Q_{\max} = 24.5 \text{ \AA}^{-1}$.

XPCS Measurements and Data Analysis. XPCS measurements were performed at DESY, at the coherence application beamline P10 at the PETRA III synchrotron source, using a photon energy of 8.4 keV set by a channel-cut Si(333) monochromator. The WAXS patterns were recorded with a PILATUS 300k detector and the XPCS was performed with a Lambda detector. The following parameters were used: 5-m sample-distance (for SAXS), 3.4- μm horizontal and 2.8- μm vertical beam focus, exposure time 1 s, and 1,000 frames per measurement point. The corresponding photon counts for the lowest flux that was used can be assessed from *SI Appendix, Fig. S5*, with an average of ~ 0.5 photons per second. The reproducibility of the observed dynamics was verified by two independent beam times, where, during the first one, multiple sample positions were recorded for each temperature (10 sample positions per temperature separated by 100 μm) and thereby averaging in space, and during the second experiment the dynamics were recorded for longer times (up to 1,000 s) for each temperature.

The dynamics are calculated using the temporal intensity autocorrelation function:

$$g_2(Q, \delta t) = \frac{1}{N} \langle I(Q, t) I(Q, t + \delta t) \rangle,$$

where δt denotes the correlation time delay, $I(Q, t)$ is the intensity at momentum transfer Q , N the normalization factor $N = \langle I(Q, t) \rangle^2$, and the $\langle \dots \rangle$ indicates the average over all frames at different times t . The 2D correlation maps were calculated by

$$C(Q, t_1, t_2) = \frac{1}{N} \langle I(Q, t_1) I(Q, t_2) \rangle,$$

where the normalization factor is given by $N = \langle I(Q, t_1) \rangle \langle I(Q, t_2) \rangle$. To estimate C in the frame $(\delta t, t)$ we apply a 45° rotation to the (t_1, t_2) system transforming it to the $(\delta t, t)$ reference frame and the corresponding maps are plotted logarithmically along δt shown in Fig. 3C.

The functional form of the double-exponential function that was used to model the temporal autocorrelation is

$$g_2(t) = A \cdot e^{-t/(2\tau_1)} + (\beta - A) \cdot e^{-t/(2\tau_2)} + c,$$

where A is the amplitude bound to the interval $[0, \beta]$, β is the contrast parameter which for the given conditions is $\beta = 0.4 \pm 0.02$, and c is the offset ranging between $[0.0, 0.02]$ which is attributed to residual scattering from streaks (*SI Appendix*). In addition, the flux dependence was investigated to ensure that the beam-induced heating is minimized (*SI Appendix*).

The Arrhenius analysis was performed by fitting the functional form $\tau(T) = A \cdot e^{E/RT}$, where R is the natural gas constant and E is the apparent activation energy; the fit results in activation barriers of 1.4 and 37.9 kJ/mol for the slow and fast component, respectively, where the component was fitted only for $T \geq 110$ K. The difference in activation barrier height reflects the different nature of the two processes as discussed here in the main text, with the latter being in fair agreement with the activation energy 34 kJ/mol obtained by dielectric measurements (9).

The normalized variance χ_T of the temporal autocorrelation function $C(Q, \delta t, t)$ is a quantitative measure of the dynamical heterogeneities (38–40), which is an experimentally accessible estimator of the four-point dynamical susceptibility χ_4 (41). The variance is calculated along axis t , by using the relation

$$\chi_T(Q, \delta t) = \frac{1}{N} \left[\langle C^2(Q, t, \delta t) \rangle_t - \langle C(Q, t, \delta t) \rangle_t^2 \right],$$

where N is the normalization parameter $N = \langle C(Q, t, \delta t = 0) \rangle^2$. The normalized

variance is shown in Fig. 4B, where the peak position follows the trend exhibited by the result of the exponential fit (the position should be $\propto e$ for a simple exponential) and the peak amplitude quantifies the heterogeneities. At $T = 89$ K, we observed a double peak, which can be related to the underlying multiple dynamical components, assigned as fast and slow dynamics in the main text. Interestingly those are not evident in the g_2 but can be seen as separate peaks in the normalized variance χ_T .

ACKNOWLEDGMENTS. We thank Thomas Blochowicz and Wojciech Roseker for comments and discussions. Parts of this research were carried out at the

1. Poole PH, Sciortino F, Essmann U, Stanley HE (1992) Phase behaviour of metastable water. *Nature* 360:324–328.
2. Palmer JC, et al. (2014) Metastable liquid-liquid transition in a molecular model of water. *Nature* 510:385–388.
3. Mishima O, Stanley HE (1998) The relationship between liquid, supercooled and glassy water. *Nature* 396:329–335.
4. Mishima O, Calvert LD, Whalley E (1985) An apparently first-order transition between two amorphous phases of ice induced by pressure. *Nature* 314:76–78.
5. Klotz S, et al. (2005) Nature of the polyamorphic transition in ice under pressure. *Phys Rev Lett* 94:025506.
6. Nelmes RJ, et al. (2006) Annealed high-density amorphous ice under pressure. *Nat Phys* 2:414–418.
7. Winkel K, Mayer E, Loerting T (2011) Equilibrated high-density amorphous ice and its first-order transition to the low-density form. *J Phys Chem B* 115:14141–14148.
8. Giovambattista N, Sciortino F, Starr FW, Poole PH (2016) Potential energy landscape of the apparent first-order phase transition between low-density and high-density amorphous ice. *J Chem Phys* 145:224501.
9. Amann-Winkel K, et al. (2013) Water's second glass transition. *Proc Natl Acad Sci USA* 110:17720–17725.
10. Kim CU, Barstow B, Tate MW, Gruner SM (2009) Evidence for liquid water during the high-density to low-density amorphous ice transition. *Proc Natl Acad Sci USA* 106:4596–4600.
11. Kim CU, Tate MW, Gruner SM (2015) Glass-to-cryogenic-liquid transitions in aqueous solutions suggested by crack healing. *Proc Natl Acad Sci USA* 112:11765–11770.
12. Tulk CA, et al. (2002) Structural studies of several distinct metastable forms of amorphous ice. *Science* 297:1320–1323.
13. Koza MM, May RP, Schober H (2007) On the heterogeneous character of water's amorphous polymorphism. *J Appl Cryst* 40:s517–s521.
14. Tse JS, Klug DD (2012) Pressure amorphized ices—an atomistic perspective. *Phys Chem Chem Phys* 14:8255–8263.
15. Limmer DT, Chandler D (2014) Theory of amorphous ices. *Proc Natl Acad Sci USA* 111:9413–9418.
16. Johari GP, Hallbrucker A, Mayer E (1987) The glass-liquid transition of hyperquenched water. *Nature* 330:552–553.
17. Handa YP, Klug DD (1988) Heat capacity and glass transition behavior of amorphous ice. *J Phys Chem* 92:3323–3325.
18. Sepúlveda A, et al. (2012) Glass transition in ultrathin films of amorphous solid water. *J Chem Phys* 137:244506.
19. Gainaru C, et al. (2014) Anomalously large isotope effect in the glass transition of water. *Proc Natl Acad Sci USA* 111:17402–17407.
20. Smith RS, Kay BD (1999) The existence of supercooled liquid water at 150 K. *Nature* 398:788–791.
21. Xu Y, Petrik NG, Smith RS, Kay BD, Kimmel GA (2016) Growth rate of crystalline ice and the diffusivity of supercooled water from 126 to 262 K. *Proc Natl Acad Sci USA* 113:14921–14925.
22. Hill CR, et al. (2016) Neutron scattering analysis of water's glass transition and micropore collapse in amorphous solid water. *Phys Rev Lett* 116:215501.
23. Andersson O (2011) Glass-liquid transition of water at high pressure. *Proc Natl Acad Sci USA* 108:11013–11016.
24. Loerting T, et al. (2015) The glass transition in high-density amorphous ice. *J Non-Cryst Solids* 407:423–430.
25. Shephard JJ, Salzmann CG (2016) Molecular reorientation dynamics govern the glass transitions of the amorphous ices. *J Phys Chem Lett* 7:2281–2285.
26. Fisher M, Devlin JP (1995) Defect activity in amorphous ice from isotopic exchange data: Insight into the glass transition. *J Phys Chem* 99:11584–11590.
27. Schober H, et al. (2000) Crystal-like high frequency phonons in the amorphous phases of solid water. *Phys Rev Lett* 85:4100–4103.
28. Brown G, Rikvold PA, Sutton M, Grant M (1997) Speckle from phase-ordering systems. *Phys Rev E Stat Phys Plasmas Fluids Relat Interdiscip Topics* 56:6601–6612.
29. Grübel G, Zontone F (2004) Correlation spectroscopy with coherent X-rays. *J Alloys Compd* 362:3–11.
30. Shpyrko OG (2014) X-ray photon correlation spectroscopy. *J Synchrotron Radiat* 21:1057–1064.
31. Sutton M, et al. (1991) Observation of speckle by diffraction with coherent X-rays. *Nature* 352:608–610.
32. Tse JS, et al. (2005) Investigation of the intermediate- and high-density forms of amorphous ice by molecular dynamics calculations and diffraction experiments. *Phys Rev B* 71:214107.
33. Finney JL, Hallbrucker A, Kohl I, Soper AK, Bowron DT (2002) Structures of high and low density amorphous ice by neutron diffraction. *Phys Rev Lett* 88:225503.
34. Dierker SB, Pindak R, Fleming RM, Robinson IK, Berman L (1995) X-Ray photon correlation spectroscopy study of Brownian motion of gold colloids in glycerol. *Phys Rev Lett* 75:449–452.
35. Bandyopadhyay R, et al. (2004) Evolution of particle-scale dynamics in an aging clay suspension. *Phys Rev Lett* 93:228302.
36. Constantin D, Davidson P, Freyssingéas É, Madsen A (2010) Slow dynamics of a colloidal lamellar phase. *J Chem Phys* 133:224902.
37. Ruta B, et al. (2012) Atomic-scale relaxation dynamics and aging in a metallic glass probed by x-ray photon correlation spectroscopy. *Phys Rev Lett* 109:165701.
38. Orsi D, Cristofolini L, Baldi G, Madsen A (2012) Heterogeneous and anisotropic dynamics of a 2D gel. *Phys Rev Lett* 108:105701.
39. Evenson Z, et al. (2015) X-ray photon correlation spectroscopy reveals intermittent aging dynamics in a metallic glass. *Phys Rev Lett* 115:175701.
40. Conrad H, et al. (2015) Correlated heterogeneous dynamics in glass-forming polymers. *Phys Rev E Stat Nonlin Soft Matter Phys* 91:042309.
41. Berthier L, et al. (2005) Direct experimental evidence of a growing length scale accompanying the glass transition. *Science* 310:1797–1800.
42. Gabriel J, Blochowicz T, Stühn B (2015) Compressed exponential decays in correlation experiments: The influence of temperature gradients and convection. *J Chem Phys* 142:104902.
43. Laage D, Hynes JT (2006) A molecular jump mechanism of water reorientation. *Science* 311:832–835.
44. Sellberg JA, et al. (2014) Ultrafast X-ray probing of water structure below the homogeneous ice nucleation temperature. *Nature* 510:381–384.
45. Ghesquière P, et al. (2015) Diffusion of molecules in the bulk of a low density amorphous ice from molecular dynamics simulations. *Phys Chem Chem Phys* 17:11455–11468.
46. Mishima O, Takemura K, Aoki K (1991) Visual observations of the amorphous-amorphous transition in H₂O under pressure. *Science* 254:406–408.
47. Mishima O, Suzuki Y (2002) Propagation of the polyamorphic transition of ice and the liquid-liquid critical point. *Nature* 419:599–603.
48. Skinner LB, Benmore CJ, Parise JB (2012) Area detector corrections for high quality synchrotron X-ray structure factor measurements. *Nucl Instrum Methods Phys Res Sect Accel Spectrometers Detect Assoc Equip* 662:61–70.
49. Skinner LB, et al. (2013) Benchmark oxygen-oxygen pair-distribution function of ambient water from x-ray diffraction measurements with a wide Q-range. *J Chem Phys* 138:074506.